

Lewis-Adduct Mediated Grain-Boundary Functionalization for Efficient Ideal-Bandgap Perovskite Solar Cells with Superior Stability

Yingxia Zong, Zhongmin Zhou, Min Chen, Nitin P. Padture,* and Yuanyuan Zhou*

State-of-the-art perovskite solar cells (PSCs) have bandgaps that are invariably larger than 1.45 eV, which limits their theoretically attainable power conversion efficiency. The emergent mixed-(Pb, Sn) perovskites with bandgaps of 1.2–1.3 eV are ideal for single-junction solar cells according to the Shockley–Queisser limit, and they have the potential to deliver higher efficiency. Nevertheless, the high chemical activity of Sn(II) in these perovskites makes it extremely challenging to control their physical properties and chemical stability, thereby leading to PSCs with relatively low PCE and stability. In this work, the authors employ the Lewis-adduct SnF₂·3FACl additive in the solution-processing of ideal-bandgap halide perovskites (IBHPs), and prepare uniform large-grain perovskite thin films containing continuously functionalized grain boundaries with the stable SnF₂ phase. Such Sn(II)-rich grain-boundary networks significantly enhance the physical properties and chemical stability of the IBHP thin films. Based on this approach, PSCs with an ideal bandgap of 1.3 eV are fabricated with a promising efficiency of 15.8%, as well as enhanced stability. The concept of Lewis-adduct-mediated grain-boundary functionalization in IBHPs presented here points to a new chemical route for approaching the Shockley–Queisser limit in future stable PSCs.

1. Introduction

Perovskite solar cells (PSCs) have emerged as a potentially disruptive photovoltaic (PV) technology that combines the merits of low cost and high power-conversion efficiency (PCE).^[1,2] Generally, PSCs employ a family of hybrid organic–inorganic halide perovskites with the general formula ABX₃, where A = CH₃NH₃⁺ (MA⁺), HC(NH₂)₂⁺ (FA⁺) or Cs⁺; B = Pb²⁺ or Sn²⁺; X = I⁻, Br⁻, or I⁻.^[3] Within this broad family of perovskites, MAPbI₃ and FAPbI₃ are the most commonly studied compositions, which exhibit relatively high optical bandgaps of 1.55 and 1.48 eV, respectively.^[4] Although

the PCE of PSCs based on MAPbI₃ and FAPbI₃ perovskites has ramped up very rapidly,^[1] the theoretically attainable PCE will be ultimately limited by their bandgaps. For achieving single-junction PSCs with the highest attainable PCE, the ideal bandgap should be 1.2–1.3 eV, as per the Shockley–Queisser limit theoretical prediction.^[4,5] Therefore, developing ideal-bandgap halide perovskite (IBHP) materials has become an emerging area of research in the PSC field, where perovskite alloying^[6] is an effective strategy for achieving this goal. In this context, Hao et al.^[7] have reported anomalous bandgap behavior in MAPb_{1-x}Sn_xI₃ alloy perovskites, and it is found that the MAPb_{0.5}Sn_{0.5}I₃-composition IBHP exhibits a bandgap of ≈1.2 eV, which allows the fabrication of PSCs with light absorption beyond 1000 nm wavelength. In another report, Zhao et al.^[8] and Liao et al.^[9] have mixed large-bandgap MAPbBr₃ and small-bandgap FASnI₃ perovskites to form (MAPbBr₃)_{0.4}(FASnI₃)_{0.6}-composition

IBHPs with a bandgap of ≈1.2 eV. Other reported IBHP compositions include MA_{0.9}Cs_{0.1}Pb_{0.5}Sn_{0.5}I₃,^[10] MAPb_{0.5}Sn_{0.5}I_{2.4}Br_{0.6},^[11] MA_{0.5}FA_{0.5}Pb_{0.75}Sn_{0.25}I₃,^[12] and FAPb_{0.5}Sn_{0.5}I₃.^[13] Very recently, we have studied systematically the alloying behavior of FAPbI₃ and CsSnI₃ perovskites, and discovered a new IBHP composition of (FAPbI₃)_{0.7}(CsSnI₃)_{0.3} that delivers an ideal bandgap of 1.3 eV.^[14] This new IBHP can also mitigate the potential thermal-stability issue due to the volatility of the MA⁺ cation and the phase-stability issue associated with the presence of the FA⁺ cation. Thus, (FAPbI₃)_{0.7}(CsSnI₃)_{0.3} is regarded as a highly promising IBHP light-absorber material for single-junction PSCs. Note that, similar perovskite compositions have also been studied in parallel by Prasanna et al.^[4] and McMeekin et al.^[15] Nevertheless, all of the aforementioned IBHP compositions contain Sn²⁺ in their crystal structures, and it is the source of the following two issues holding back the realization of the full potential of these IBHPs. First, the formation energy of Sn vacancies in the perovskite structure is very low, which can induce metallic conductivity in these materials that is highly undesirable for the PSC device operation.^[16,17] Second, Sn(II) is much less tolerant of environmental stresses (air, moisture, light, etc.) compared to Pb(II), resulting in the more rapid degradation of those IBHPs.^[17]

Y. Zong, M. Chen, Prof. N. P. Padture, Prof. Y. Zhou
School of Engineering
Brown University
Providence, RI 02912, USA
E-mail: nitin_padture@brown.edu; yuanyuan_zhou@brown.edu
Dr. Z. Zhou
Department of Chemistry
The University of Tokyo
Tokyo 113-0033, Japan

DOI: 10.1002/aenm.201800997

Herein we demonstrate grain-boundary functionalization as a new way to enhance the physical properties and chemical stability of IBHPs, and correspondingly achieve high-performance ideal-bandgap PSCs. We have discovered that, by incorporating a new Lewis-adduct— $\text{SnF}_2 \cdot 3\text{FACl}$ —in the solution-processing of $(\text{FAPbI}_3)_{0.7}(\text{CsSnI}_3)_{0.3}$ IBHP thin films, all the perovskite grains can be coated with uniform layers of low-crystallinity SnF_2 . The highly continuous SnF_2 phase at the grain-boundaries not only suppresses the formation of intrinsic Sn vacancies in the IBHP thin film, but also forms an encapsulation layer for individual perovskite grains at the nanoscale. This encapsulation layer serves as a barrier for the moisture/oxygen ingress as well as the thermal/light induced decomposition in the IBHP thin films. The resultant PSCs show PCE up to 15.8%. Excellent stability is also demonstrated, with 90.0% and 98.3% retention of the initial PCE after 288-h storage in the ambient and inert atmospheres, respectively.

2. Results and Discussion

2.1. Mechanisms of Lewis-Adduct Mediated Grain-Boundary Functionalization

Figure 1a illustrates schematically the formation process of the IBHP thin films with SnF_2 at the grain boundaries. The $\text{SnF}_2 \cdot 3\text{FACl}$ complex and IBHP precursors are simply mixed and co-dissolved in a polar solvent (dimethylformamide or DMF), forming a solution ready for the “one-step” spin-coating processing. The antisolvent (chlorobenzene) dripping protocol is employed to induce the rapid crystallization of highly uniform IBHP thin films. Along with IBHP crystallization, the $\text{SnF}_2 \cdot 3\text{FACl}$ phase is also expected to precipitate preferentially at IBHP grain boundaries, considering the relatively small amount of $\text{SnF}_2 \cdot 3\text{FACl}$ in the whole composite system, as well as the “soft” nature of $\text{SnF}_2 \cdot 3\text{FACl}$ (as discussed later). The initially crystallized IBHPs exhibit fine-grain structure due to the rapid nucleation rate under the room-temperature antisolvent treatment,^[3,18] which is similar to what has been observed in other perovskites. The second step entails simple thermal annealing, which converts $\text{SnF}_2 \cdot 3\text{FACl}$ to SnF_2 , and also results in the significant coarsening of the IBHP grains. Through this process, the grain-boundary network in the resultant IBHP thin film is not only fully passivated by continuous SnF_2 phases, but also has a significantly reduced density.

The $\text{SnF}_2 \cdot 3\text{FACl}$ Lewis-adduct is synthesized by co-dissolving SnF_2 and FACl in the molar ratio of 1:3 in DMF, followed by precipitation from the solution. Interestingly, as shown in Figure 1b, $\text{SnF}_2 \cdot 3\text{FACl}$ exhibits a semisolid state at room temperature, which is clearly different from the particulate SnF_2 solid. And upon mild heating (at ≈ 80 °C), $\text{SnF}_2 \cdot 3\text{FACl}$ quickly undergoes a reversible transition to the liquid state (Figures S1 and S2, Supporting Information) due to its low melting point. For comparison, the melting point of SnF_2 is as high as 215 °C. The X-ray diffraction (XRD) pattern of $\text{SnF}_2 \cdot 3\text{FACl}$ (at room temperature) is presented in Figure S3 of the Supporting Information, showing diffraction peaks that are clearly different from those for SnF_2 and FACl phases. This indicates that $\text{SnF}_2 \cdot 3\text{FACl}$ is a completely new phase, and it is

not a simple mixture of SnF_2 and FACl. Note that the exact crystalline structure of $\text{SnF}_2 \cdot 3\text{FACl}$ remains to be resolved in our future studies. In fact, as shown in Figure S4 of the Supporting Information, we find that SnF_2 alone exhibits very low solubility in DMF, whereas the same molar amount of $\text{SnF}_2 \cdot 3\text{FACl}$ dissolves in the DMF easily. This phenomenon indicates that there is strong Lewis base-acid interaction between SnF_2 and FACl, which is key to the formation of the new $\text{SnF}_2 \cdot 3\text{FACl}$ complex phase. Figure S5 of the Supporting Information presents a Fourier-transform infrared (FTIR) spectrum of $\text{SnF}_2 \cdot 3\text{FACl}$. With the presence of Lewis-acid SnF_2 , the $\nu(\text{C}=\text{N})$ is lowered from 1100 to 1080 cm^{-1} ,^[19] confirming the coordination of FACl with SnF_2 . Such coordination is not stable at elevated temperatures, and therefore, upon thermal annealing (100 to 200 °C), $\text{SnF}_2 \cdot 3\text{FACl}$ first melts quickly, and then decomposes to SnF_2 accompanied by the release of FACl byproduct according to:

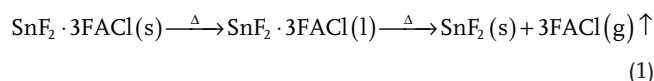


Figure S6 of the Supporting Information presents an SEM image of the SnF_2 film that is converted from a solution-coated $\text{SnF}_2 \cdot 3\text{FACl}$ film, showing a fully dense SnF_2 microstructure. The pure SnF_2 phase is confirmed using XRD (Figure S7, Supporting Information). For comparison, SnF_2 film that is solution-coated using the SnF_2 solution (or suspension) in DMF shows nonuniform coverage on the substrate, as seen in Figure S8 of the Supporting Information. Thus, the combination of the characteristics such as high-solubility, unique state (semisolid at RT and liquid at elevated temperatures), and phase-pure nature of the $\text{SnF}_2 \cdot 3\text{FACl}$ complex contributes to the uniform distribution of $\text{SnF}_2 \cdot 3\text{FACl}$ phase along the grain boundaries in the IBHP thin films. Furthermore, the controlled morphological evolution of SnF_2 from the transformation of the $\text{SnF}_2 \cdot 3\text{FACl}$ complex is key to the formation of the continuous SnF_2 -functionalized grain boundaries in the final IBHP thin films. For comparison, in the case where SnF_2 is used instead of $\text{SnF}_2 \cdot 3\text{FACl}$, as shown schematically in Figure S9 of the Supporting Information, SnF_2 phase first precipitates in the early stage of solution supersaturation due to its relatively low solubility in the solvent, which serves as heterogeneous nucleation sites for the subsequent IBHP crystallization. This naturally leads to the formation of an IBHP thin film with a much higher-density GB network. Meanwhile, the SnF_2 phase segregate locally in the IBHP thin film, owing to the rigid nature of the SnF_2 crystals/particles. Since the incorporation of SnF_2 through this conventional method has shown some promise in improving perovskite thin-film properties and device performance,^[20] this study focuses on achieving controllable SnF_2 incorporation while minimizing the detrimental side effects.

Figure 1c–f is top-view scanning electron microscope (SEM) images of the $\text{SnF}_2 \cdot 3\text{FACl}$ -incorporated IBHP thin films (on PEDOT:PSS-coated ITO substrate that is used for making devices) with annealing (at 170 °C) durations of 0, 20, 60, and 120 s. The grain-size statistics, as measured using image analyses of the SEM images, for the three thin films are presented in Figure S10 of the Supporting Information. As seen in Figure 1c, the IBHP thin film before annealing is composed

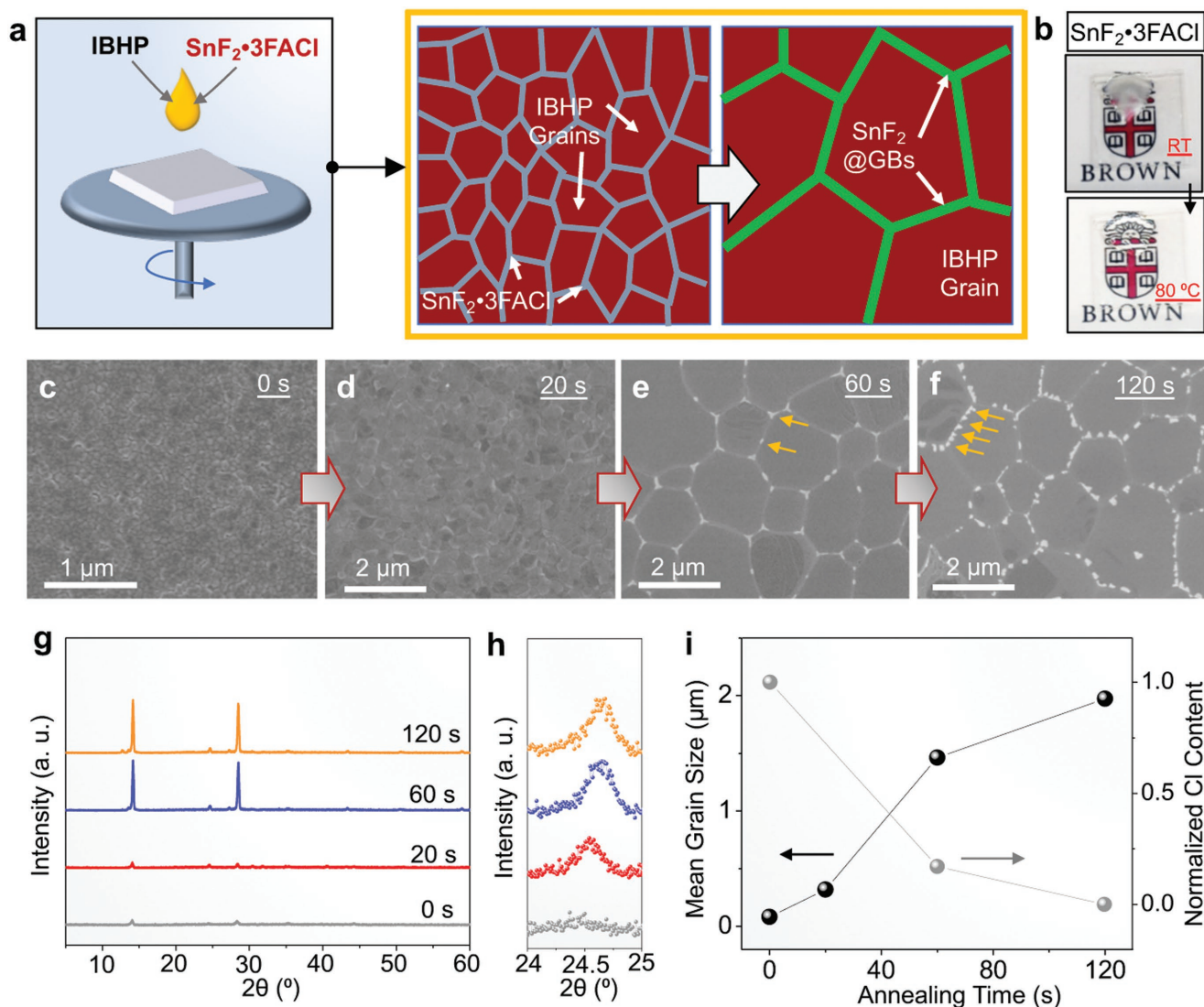


Figure 1. Mechanisms of Lewis-adduct-mediated grain-boundary functionalization of IBHP thin films. a) Schematic illustration showing the processing and microstructural evolution in IBHP thin films with the incorporation of the $\text{SnF}_2 \cdot 3\text{FACl}$ Lewis-adduct in the precursor solution. b) Photographs of the $\text{SnF}_2 \cdot 3\text{FACl}$ phase at room temperature (RT) and upon mild heat-treatment (80°C). Top-view SEM images showing the morphology of spin-coated IBHP thin films with $\text{SnF}_2 \cdot 3\text{FACl}$ after thermal annealing at 170°C for: c) 0 s, d) 20 s, e) 60 s, and f) 120 s. g, h) Corresponding XRD patterns. i) Plots of the grain size and Cl-content in the IBHP thin films as a function of annealing time.

of particle-like grains of ≈ 82 nm average size, with relatively ill-defined grain boundaries. The incorporated $\text{SnF}_2 \cdot 3\text{FACl}$ phases are not immediately distinguishable at the grain boundaries, which indicates good dispersion of the small amount of $\text{SnF}_2 \cdot 3\text{FACl}$ throughout the whole thin film. The energy-dispersive spectroscopy (EDS) spectrum (Figure S11, Supporting Information) of the IBHP sample at this stage shows Sn, F, and Cl signals confirming the presence of the $\text{SnF}_2 \cdot 3\text{FACl}$ phases in the thin film. After 20 s annealing, the grain boundaries and the triple-junctions become more visible, and the IBHP grains become larger (Figure 1d). At 60 s, the average grain size increases to $\approx 1.5 \mu\text{m}$ (Figure 1e). Meanwhile, it is found that a new phase (confirmed to be SnF_2 later) forms at the grain boundaries of IBHPs. After 120-s annealing, the grain growth stagmates (Figure 1f), showing a similar average grain size ($\approx 1.9 \mu\text{m}$)

to that in Figure 1e. However, the SnF_2 phase becomes much more prominent, forming near-continuous coating along all of the grain boundaries. The XRD patterns that correspond to the SEM images in Figure 1c–f, respectively, are shown in Figure 1g, h. In all four samples, only those diffraction peaks associated with the IBHP phase are observed. The absence of XRD peaks associated with crystalline $\text{SnF}_2 \cdot 3\text{FACl}$ and/or SnF_2 phases could be due to the small amount of the phases and their poor crystallinity. The variation of the intensity and the full-width at half-maximum (FWHM) of the characteristic peak (Figure 1h) for IBHP is plotted as a function of the annealing time in Figure S12 of the Supporting Information. It is clear that the intensity of the 111 peak increases and the FWHM decreases when the annealing time increases to 60 s. Further annealing does not result in any notable changes in the XRD pattern.

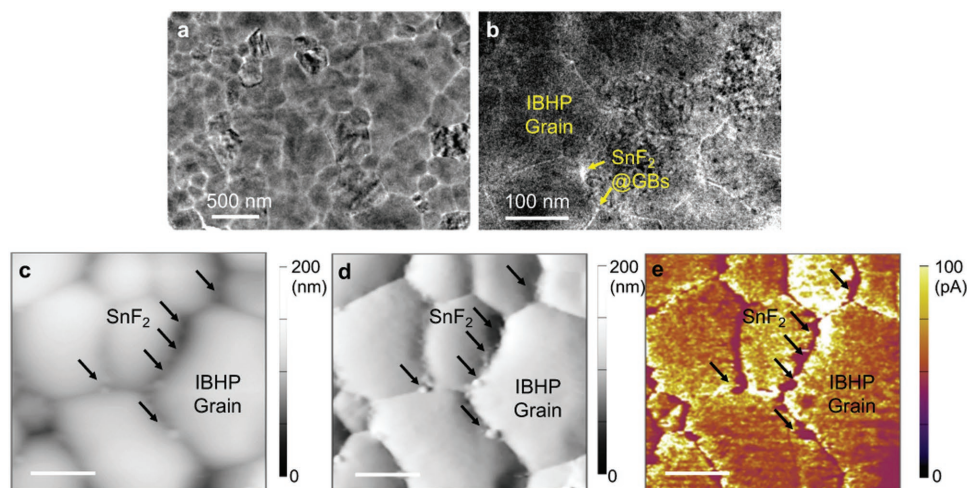


Figure 2. TEM and c-AFM imaging of grains and grain boundaries in IBHP thin films. Bright-field TEM images of an IBHP thin film processed with $\text{SnF}_2\cdot 3\text{FACl}$ at a) lower magnification and b) higher magnification. c-AFM maps (scale bar: 250 nm) of an IBHP thin film processed with $\text{SnF}_2\cdot 3\text{FACl}$: c) topography, d) deflection, and e) current. Note that the differences in the grain sizes in the TEM and AFM images are due to the specific substrates used for the deposition of the IBHP thin films for the TEM and the AFM experiments (see the Experimental Section).

These results are consistent with the grain-growth behavior observed in the SEM. The slight shift of 111 peak toward high 2θ angle with longer annealing is related to the increase in the crystallinity. In Figure 1i, the grain size and Cl-content (determined using EDS) in the thin film are plotted as a function of annealing time. It is found that the Cl-content is gradually reduced to zero with increasing annealing time, which suggests that the grain growth is driven by the $\text{SnF}_2\cdot 3\text{FACl}$ -to- SnF_2 phase conversion. The EDS measurement of the final IBHP thin film confirms the presence of F. The indispensable role of the FACl component on the grain growth is further supported by the fact that similar grain-growth behavior occurs when only FACl is used as an additive during the solution processing (see Figure S13, Supporting Information). Such FACl-mediated perovskite grain growth is consistent with the previous studies reported by us^[21] and others^[22] in the literature. We have further prepared a control IBHP thin film sample by employing only SnF_2 as the additive in the solution processing, and the top-view SEM surface morphology of this thin film is shown in Figure S14 of the Supporting Information. As expected, heterogeneously segregated SnF_2 particles/crystals are observed in those IBHP thin films. As a result, the average IBHP grain size of this thin film is only ≈ 220 nm (Figure S15, Supporting Information), and the XRD peak intensity of this thin film is significantly lower than that of the IBHP thin film processed with $\text{SnF}_2\cdot 3\text{FACl}$ (see Figure S16, Supporting Information). These observations are consistent with the schematic illustrations in Figure 1a and Figure S6 (Supporting Information).

2.2. Microscopic Characterization of Perovskite Thin Films

For revealing and confirming the detailed microstructure in the final IBHP thin film processed with $\text{SnF}_2\cdot 3\text{FACl}$, transmission electron microscopy (TEM) studies were performed. For the TEM-specimen preparation, IBHP thin films were

solution-deposited directly on the TEM grid. This method has been previously applied and proven suitable for TEM studies of perovskite materials.^[23] Note that while the exact grain size in the IBHP TEM sample can be different from that deposited on the PEDOT:PSS-coated ITO substrate due to differences in the specific wetting behavior of the precursor solution on the TEM grid,^[24] the general microstructure characteristics of the thin film TEM sample are similar to the thin film that is deposited on the PEDOT:PSS-coated ITO substrate. Figure 2a,b shows TEM images of the final IBHP thin film at higher and lower magnifications, respectively. The highly crystalline IBHP grains and the low-crystallinity SnF_2 phases can be distinguished easily from the contrast in the images. The low-contrast SnF_2 phases appear to be highly continuous along the grain boundaries. We have also observed that the IBHP studied here is more electron-beam-sensitive than MAPbI_3 , precluding more detailed microstructure/composition analysis using the TEM. (Note that low-dose TEM techniques are being developed for the characterization of a broad range of halide perovskites which may solve this issue in the future.) Bearing this in mind, we have further performed conductive atomic force microscopy (c-AFM) to confirm phases indirectly.

Figure 2c,d shows c-AFM results from the characterization of the final IBHP thin film. In the topography and deflection images in Figure 2c,d the second phases can be easily identified at the IBHP grain boundaries regions, while the IBHP grain surfaces appear smooth. In the current map in Figure 2e, the grain-boundary regions show conductivity several orders of magnitude lower than that of the IBHP grains. Since there is a substantial difference in the conductivities of the insulating SnF_2 and the semiconducting IBHP phases, the c-AFM results indicate that the grain-boundary phases are SnF_2 . To further confirm this, c-AFM characterization has also been performed on an IBHP thin film processed with only FACl, showing typical grain boundary and grain features without any secondary phases (see Figure S17, Supporting Information). Thus, all the

TEM and the c-AFM results are consistent with the SEM results, confirming the success in preparing IBHP thin films with the targeted microstructure shown schematically in Figure 1a.

2.3. Physical Properties of Perovskite Thin Films

The absorption spectra of the IBHP thin films processed with and without $\text{SnF}_2 \cdot 3\text{FACl}$ are compared in Figure 3a. It is found that light absorption is enhanced at all wavelengths in the IBHP thin film processed with $\text{SnF}_2 \cdot 3\text{FACl}$, which can be attributed to the beneficial effects of high crystallinity and low-density grain boundaries in that film. The derived Urbach energy from the absorption tails are 17 and 55 meV for the IBHP thin films processed with and without $\text{SnF}_2 \cdot 3\text{FACl}$, respectively. This suggests that the defect density in the IBHP thin film is significantly reduced when $\text{SnF}_2 \cdot 3\text{FACl}$ is used. Figure 3b shows the photoluminescence (PL) spectra of both thin films. It is interesting that the intensity of the PL emission is reduced in the IBHP thin film processed with $\text{SnF}_2 \cdot 3\text{FACl}$. In this context, it has been shown that the PL emission in Sn(II)-based perovskites is proportional to the concentration of Sn vacancies in the materials.^[16] Also, theoretical calculations suggest that the Sn vacancies in the final perovskites can be suppressed when the Sn(II)-based perovskites are grown in Sn(II)-rich conditions.^[25] Thus, the observed PL reduction in the IBHP thin film

processed with $\text{SnF}_2 \cdot 3\text{FACl}$ is most likely due to the reduced Sn-vacancy concentration in the IBHP. We have further measured the space-charge-limited-current evolution (in the dark) of both thin films as a function of bias voltage in capacitor-like devices in the FTO/IBHP/Au configuration. The results are shown in Figure 3c, where the IBHP thin film processed without $\text{SnF}_2 \cdot 3\text{FACl}$ exhibits almost quasi-ohmic I - V behavior. This is expected as the high concentration of Sn vacancies can lead to metallic conductivity. The kink point (where the current increases linearly and then nonlinearly) in the I - V curve, which marks the onset of the trap-filling process,^[26] is not observed until a high bias of about 0.6 V is applied. But, the grain-boundary-functionalized IBHP thin film exhibits typical I - V behavior of semiconductors showing a space-charge-limited current evolution. The trap-filled limited voltage is significantly reduced to less than 0.3 V, which confirms the reduction of Sn vacancies in the thin film. Figure 3d illustrates schematically the proposed mechanisms of the Sn(II) F_2 functionalization layer in reducing the Sn vacancies within the IBHP grains: it is likely that the high concentration of Sn(II) ions diffuse into the IBHP grains from the grain boundaries, annihilating the Sn vacancies. In addition to the Sn-vacancy induced trap states in bulk IBHP grains, the grain boundaries in the IBHP thin films are another region where trap states accumulate. In the IBHP thin film processed with $\text{SnF}_2 \cdot 3\text{FACl}$, the grain-boundary density is significantly lower, and the grain boundary

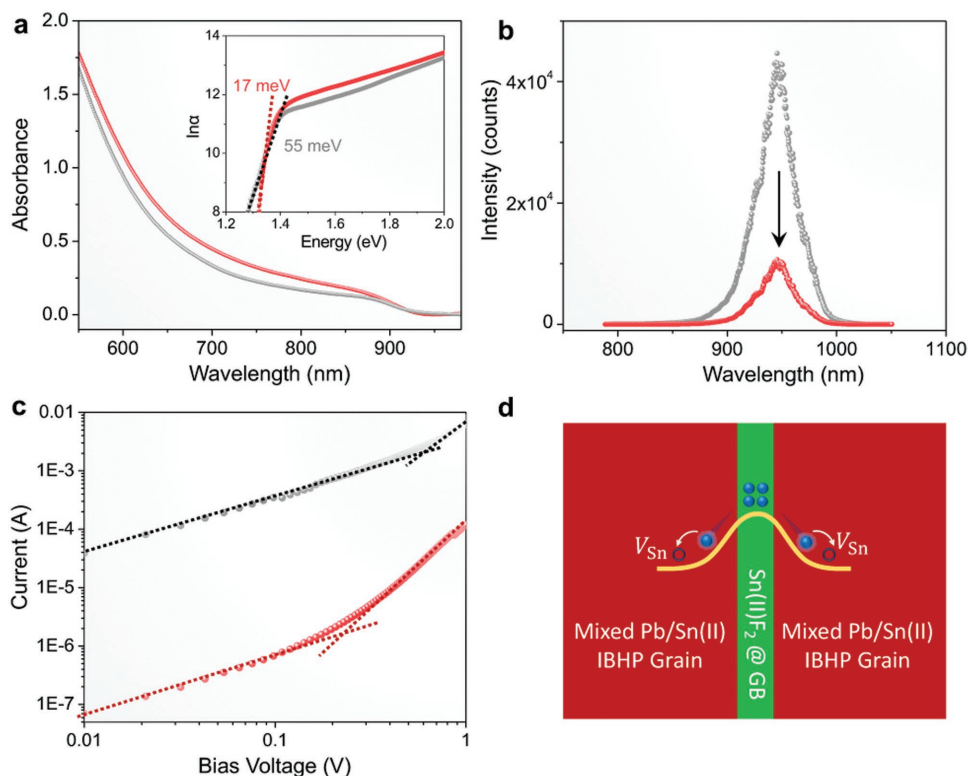


Figure 3. Physical properties of perovskite thin films. a) UV-vis spectra of IBHP thin films processed with (red) and without (gray) $\text{SnF}_2 \cdot 3\text{FACl}$. Inset shows estimation of the Urbach energy for both samples. b) Steady-state PL spectra of the IBHP thin films processed with (red) and without (gray) $\text{SnF}_2 \cdot 3\text{FACl}$. c) Space-charge limited current evolution as a function of bias voltage, measured using capacitor-like devices in the FTO/IBHP/Au configuration for IBHP thin films processed with (red) and without (gray) $\text{SnF}_2 \cdot 3\text{FACl}$. d) Schematic illustration of the effect of the Sn(II)F_2 grain-boundary functionalization in modulating Sn-vacancies in IBHP grains.

are continuously passivated. Therefore, it is expected that the trap density at IBHP grain boundaries are also reduced. It is still challenging to quantify the contribution of Sn-vacancy suppression and grain-boundary reduction/passivation toward the trap-density reduction, which is a topic of our future research.

2.4. Solar-Cell Performance of Perovskite Thin Films

PSCs were fabricated to evaluate the PV performance of the IBHP thin film processed with $\text{SnF}_2 \cdot 3\text{FACl}$. A reference solar cell is made with the neat IBHP thin film processed without any additives. **Figure 4a** shows schematically the device architecture that is used in this study. The typical current density–voltage (J – V) curves (reverse scan) of the PSC devices are compared in **Figure 4b** and the extracted PV performance parameters are

shown in the inset. The PSC processed with $\text{SnF}_2 \cdot 3\text{FACl}$ shows enhanced overall PCE of 14.7% compared with 12.9% PCE for the additive-free case. The short-circuit current densities (J_{SC}) for the IBHP thin film processed with and without $\text{SnF}_2 \cdot 3\text{FACl}$ are 26.34 and 24.41 mA cm^{-2} , respectively. Such high J_{SC} values are attributed to the lower bandgap (1.3 eV) in IBHPs compared with those (1.4–1.6 eV) in the widely studied MAPbI_3 and FAPbI_3 perovskites. There are also obvious improvements in open-circuit voltage (V_{OC}), from 0.68 to 0.70 V, and fill factor (FF) from 0.777 to 0.797 when IBHP thin films are processed with $\text{SnF}_2 \cdot 3\text{FACl}$. The PCE statistics are shown in **Figure 4c**, which confirms the reproducibility of the overall PCE improvement.

All these device results are consistent with the reduced trap density and Sn-vacancy concentration in the IBHP thin film processed with $\text{SnF}_2 \cdot 3\text{FACl}$. The typical J – V curves of PSCs using IBHP thin films processed with only SnF_2 and only

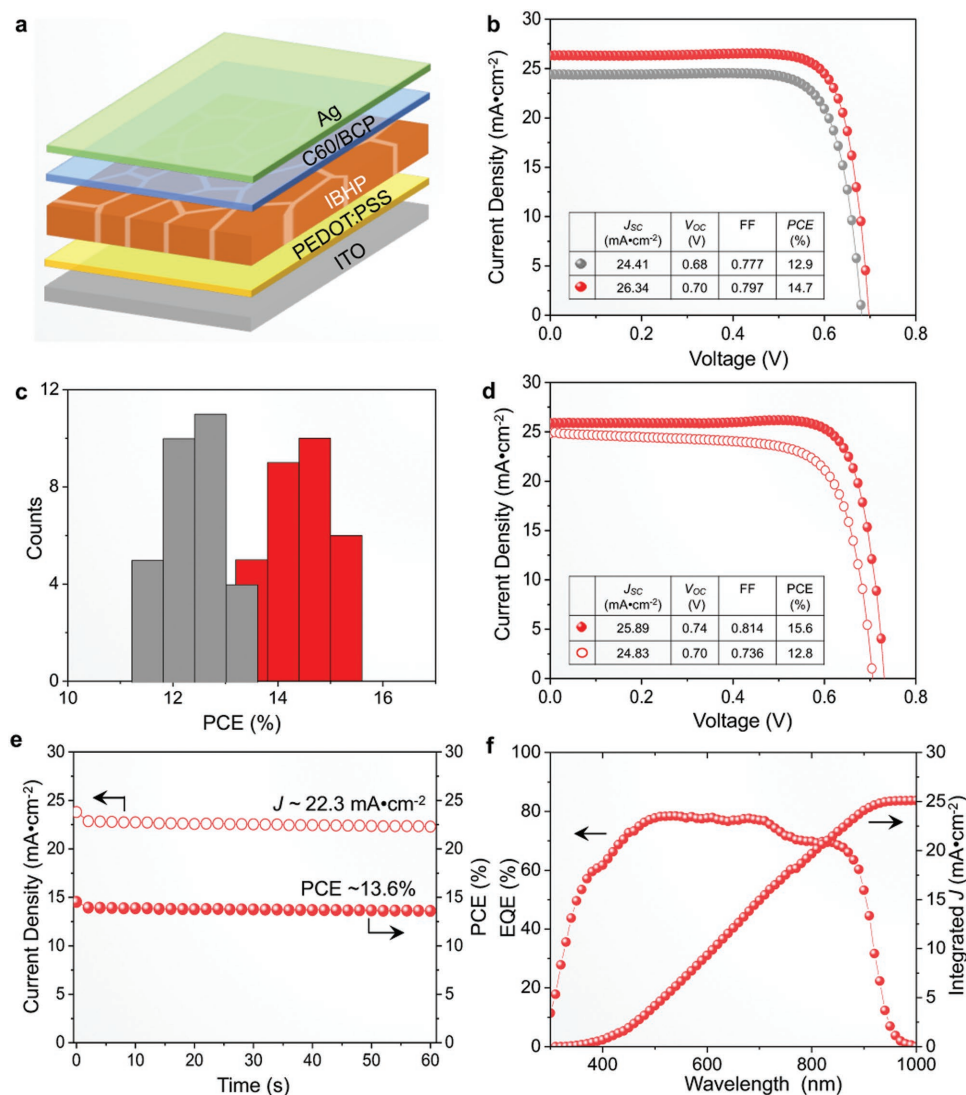


Figure 4. PV performance of perovskite thin films. a) Schematic illustration of the device architecture of PSCs. b) Typical J – V curves (reverse scan) and PV performance parameters (inset) and c) PCE statistics of the PSCs based on IBHP thin films processed with (red) and without (gray) $\text{SnF}_2 \cdot 3\text{FACl}$. “Champion” PSC based on the IBHP thin film processed with $\text{SnF}_2 \cdot 3\text{FACl}$. d) J – V hysteresis in reverse (open symbols) and forward (solid symbols) scans together with PV performance parameters (inset), e) maximum-power-point current (open symbols) and PCE (solid symbols) outputs, and f) EQE spectrum.

FAcI in the same molecular amount, both of which show lower overall PCE (see Figure S18, Supporting Information). This further confirms the significance of using the Lewis-adduct $\text{SnF}_2 \cdot 3\text{FAcI}$ in the processing IBHP thin films for the combined effects of continuous grain-boundary functionalization and reduction in the grain-boundary network density. Figure 4d shows J - V curves (in both reverse and forward scans) of the PSC using IBHP thin films processed with $\text{SnF}_2 \cdot 3\text{FAcI}$. This device shows typical photocurrent hysteresis. This may be related to the thin-film device-architecture and IBHP composition that is used in this study, as the additive-free PSC also exhibits similar hysteresis (Figure S19, Supporting Information). The J - V curve of the “champion” cell made using the IBHP thin film processed with $\text{SnF}_2 \cdot 3\text{FAcI}$ is presented in Figure 4d, which shows 15.8% PCE. The stabilized PCE output at the maximum power point (Figure 4e) is 13.6%, which compares favorably with the PCE extracted from the J - V curve. The external quantum efficiency (EQE) spectrum for the same “champion” cell is shown in Figure 4f, where the integrated current density (25.2 mA cm^{-2}) is close to the value extracted from the J - V measurements (Figure 4d inset).

2.5. Environmental Stability of Perovskite Thin Films and Solar Cells

The IBHP thin film processed with $\text{SnF}_2 \cdot 3\text{FAcI}$ also exhibit enhanced chemical stability upon exposure to key environmental stresses (moisture, thermal, light). Figure 5a–c shows comparison of XRD patterns before and after exposure to certain stresses. Moisture stress is applied by storing the thin film in a climate chamber with controlled humidity (70% RH) for 46 h at room temperature. Thermal stress is applied by annealing the thin films on the hotplate at $200 \text{ }^\circ\text{C}$ for 3 h in the

nitrogen-filled glovebox. Light stress is applied by continuous exposure to AM 1.5G one-sun intensity simulated sunlight for 23 h on a sample that is sealed in a poly(methylmethacrylate) layer (for minimizing other environmental effects). As seen in Figure 5a–c, after applying the same stresses, the IBHP thin films processed with $\text{SnF}_2 \cdot 3\text{FAcI}$ retain the pure perovskite phase, whereas the reference thin films have degraded significantly to PbI_2 . Such degradation in the neat IBHP thin film can be a combined effect from the hygroscopic, volatile behavior of the FA^+ cations, and the chemical sensitivity of Sn^{2+} cation, which leads to the collapse of the perovskite structure. While the exact degradation mechanisms are unclear in the complex-composition IBHP thin films at this time, it is clear that the continuous grain-boundary passivation, the reduced grain-boundary density, and the Sn(II)-rich grain-boundary regions all contribute together toward the significant improvements in the environmental stability of the IBHP thin films.

The stability of PSCs processed with and without $\text{SnF}_2 \cdot 3\text{FAcI}$ are also compared. After 288 h storage in ambient conditions (20% RH, RT, ambient light), the PSC processed with $\text{SnF}_2 \cdot 3\text{FAcI}$ retains 90.0% of the initial PCE, whereas the PSC processed without $\text{SnF}_2 \cdot 3\text{FAcI}$ shows rapid decay (76.7% retention after 216 h) in PCE once exposed to ambient atmosphere, and even fails to operate after 216-h storage. In particular, there is almost no performance decay after 288 h (98.3%), when the PCS processed with $\text{SnF}_2 \cdot 3\text{FAcI}$ is stored in inert atmosphere (nitrogen-filled glovebox), attesting to the intrinsic stability of the thin film and PSC. While more standard tests will be conducted in the future for fully evaluating the device stability of these PSCs,^[27] the achieved stability in IBHP solar cells is comparable with that in the state-of-the-art devices reported in the literature.^[8,11] The combination of the thin-film and PSC stability results clearly demonstrate the advantage of the Lewis-adduct

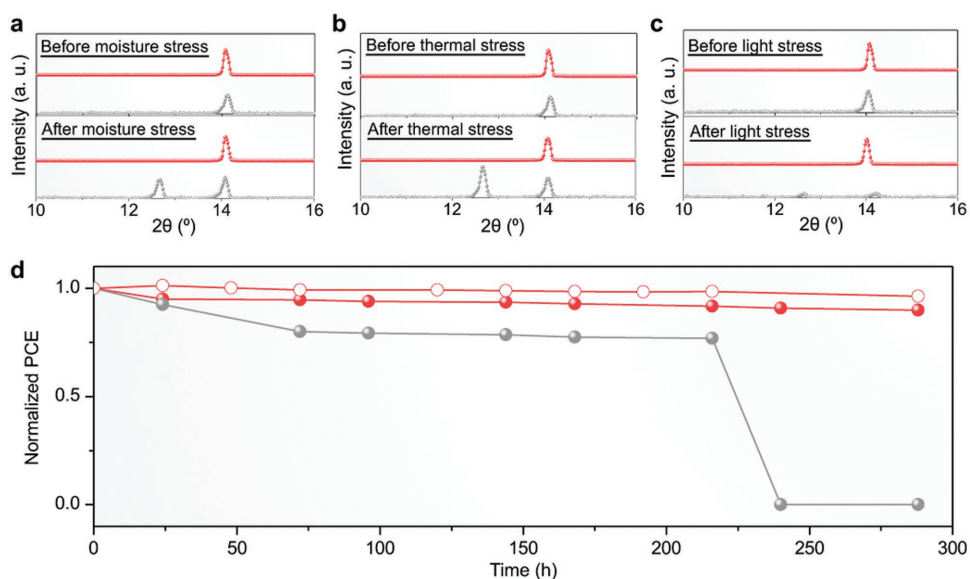


Figure 5. Stability of perovskite thin films and devices. XRD patterns of IBHP thin films processed with (red) and without (gray) $\text{SnF}_2 \cdot 3\text{FAcI}$ before/after exposure to environmental stresses: a) moisture, b) thermal, and c) light. (See text for test conditions details.) d) PCE evolution of PSC devices processed with (red, solid) and without (gray, solid) $\text{SnF}_2 \cdot 3\text{FAcI}$ upon storage in the ambient conditions (20% RH, $25 \text{ }^\circ\text{C}$, ambient light), and the PSC devices (red, open) processed with $\text{SnF}_2 \cdot 3\text{FAcI}$ upon storage in the inert conditions (nitrogen-filled glovebox).

$\text{SnF}_2 \cdot 3\text{FACl}$ -mediated grain-boundary functionalization in achieving significantly improved stability in IBHP-based PSCs.

3. Conclusion

We have demonstrated the successful engineering of grain-boundaries in IBHP thin films. We show that by incorporating the $\text{SnF}_2 \cdot 3\text{FACl}$ Lewis-adduct in the IBHP precursor solution, grain boundaries in the resulting IBHP thin films are continuously functionalized by SnF_2 , forming a Sn(II)-rich grain boundary network. The controlled evolution of SnF_2 phase by the $\text{SnF}_2 \cdot 3\text{FACl} \rightarrow \text{SnF}_2$ conversion is key to the success of continuous grain-boundary functionalization approach. This approach also assists in the growth of the grains in the IBHP thin films, further reducing the grain-boundary network density. In this regard, the IBHP thin films with continuous Sn(II)-rich grain boundaries exhibit reduced Sn-vacancy concentration and trap-density. The chemical stability of the functionalized IBHP thin films is also significantly improved due to the protection of IBHP grains by the SnF_2 -containing grain boundaries that serve as nanoscale “shells.” Furthermore, the enhancement of the physical properties and chemical stability of the IBHP thin films contributes to the increase in the device PCE and stability. We envision that the grain-boundary functionalization approach presented here represents an important generic strategy for improving ideal-bandgap PSCs, which is likely to have an impact in realizing the theoretical limit of PSCs in the future.

4. Experimental Section

Materials/Film Synthesis: The $(\text{FAPbI}_3)_{0.7}(\text{CsSnI}_3)_{0.3}$ IBHP precursor solution (40 wt%) was prepared by co-dissolving 76.1 mg FAI (Dyesol, Australia), 203.9 mg PbI_2 (99.9985% pure, Alfa Aesar, USA), 49.3 mg CsI (99.999% pure, Sigma-Aldrich, USA), and 70.7 mg SnI_2 (99.999%, Sigma-Aldrich, USA) in 600 mg DMF (99.8% pure, Sigma-Aldrich, USA). $\text{SnF}_2 \cdot 3\text{FACl}$ was synthesized by mixing SnF_2 and FACl (Sigma-Aldrich, USA) in DMF in molar ratio 1:3, followed by recrystallization. To the $(\text{FAPbI}_3)_{0.7}(\text{CsSnI}_3)_{0.3}$ IBHP solution 12.6 mg $\text{SnF}_2 \cdot 3\text{FACl}$ (5 mol% of the IBHP molar amount in the solution) was added. Note that the amount of $\text{SnF}_2 \cdot 3\text{FACl}$ added to the IBHP solution was optimized based on the PCE of the resulting PSCs. After stirring for 2 h at room temperature, the solutions became clear, and they were spin-coated at 4000 rpm for 30 s, during which 600 μL of anhydrous chlorobenzene (Sigma-Aldrich, USA) was quickly dripped at the center of the substrates at 10 s after the start of spin-coating. The thin films were then transferred to a hotplate and annealed at 170 °C for different time durations according to the experimental need. The whole synthesis process was conducted in the nitrogen-filled glovebox.

Materials Characterization: XRD patterns were obtained using $\text{Cu K}\alpha_1$ radiation ($\lambda = 0.15406$ nm) with a step size of 0.02° on an X-ray diffractometer (Smartlab, Rigaku, Japan). The surface morphology of the thin films was characterized using SEM (Magellan 400L, FEI, Germany; LEO 1530VP, Carl Zeiss, Germany). EDS data were acquired using the EDS detector attached to the FEI SEM. The c-AFM measurements were performed using a versatile AFM (MFP-3D Origin, Asylum Research, USA) in contact mode using a conducting platinum-coated silicon probe (Econo-SCM-PIC, Asylum Research, USA). The thin film used for the c-AFM measurement was deposited on an FTO substrate. High-resolution characterization was performed using a TEM

(2100F, JEOL, Japan) operated at 200 kV accelerating voltage. TEM specimens were prepared using the same procedure as above directly on a TEM grid (SPI, USA) which served as the substrate. UV-vis spectra were obtained using a spectrophotometer (UV-2600, Shimadzu, Japan) equipped with an integrating sphere attachment (ISR-2600, Shimadzu, Japan). FTIR spectra were obtained on a spectrometer (4100, Jasco Instruments, USA). The samples for the FTIR measurements were prepared by scratching the thin films from the substrates. The steady-state PL spectra were recorded using an in-house spectrophotometer under 395 nm excitation.

Device Fabrication and Testing: The PSC devices were fabricated in the configuration of ITO/PEDOT:PSS/IBHP/C60/BCP/Ag. ITO-coated glass substrates ($15 \Omega \text{ sq}^{-1}$, Techno Print, Japan) were cleaned sequentially by sonication in detergent and deionized water, acetone, isopropanol, and ethanol for 10 min each. After drying under a N_2 stream, substrates were further cleaned by exposing them to plasma for 15 min. The PEDOT:PSS (Baytron P VP Al 4083 filtered through a $0.45 \mu\text{m}$ Nylon filter) hole-transporting layer with a thickness of ≈ 30 nm was spin-coated onto ITO substrates at 5000 rpm for 30 s and annealed at 150 °C for 10 min in air. The substrates were then transferred to a nitrogen-filled glove box. $(\text{FAPbI}_3)_{0.7}(\text{CsSnI}_3)_{0.3}$ IBHP thin film was then deposited using the procedure described above. The best-performing devices were fabricated with some modifications in processing parameters for optimizing the grain boundary structures. Here, a mixed solvent of DMF/DMSO (4:1 v/v) is used for making the solution. The IBHP precursor solutions were spin-coated on the substrates at 1000 rpm for 10 s followed by 4000 rpm for 30 s, in which 800 μL of chlorobenzene was quickly dripped at the center of the substrates after 12 s, and annealed at 150 °C for 10 min. Finally, C60 (30 nm)/Bathocuproine (BCP, 10 nm)/Ag (100 nm) were sequentially deposited by thermal evaporation to complete the PSC device. J - V characteristics were measured under AM1.5G one-sun illumination (100 mW cm^{-2}) using a solar simulator (Sumitomo Heavy Industries Advanced Machinery, Japan) at 0.01 V per step with a delay time of 50 ms in both forward ($J_{\text{SC}} \rightarrow V_{\text{OC}}$) and reverse ($V_{\text{OC}} \rightarrow J_{\text{SC}}$) scans. The typical standard device area is 0.09 cm^2 that is defined by a nonreflective metal mask. The light intensity of the solar simulator was calibrated using a standard silicon solar cell (PV Measurements, USA). Stabilized PCE outputs at maximum-power-points of the reverse-scan J - V curves are typically monitored for confirming the PCE. EQE spectra were measured on a quantum-efficiency system (QE-R, Enlitech, Taiwan) under DC power mode.

Supporting Information

Supporting Information is available from the Wiley Online Library or from the author.

Acknowledgements

Y.Z. and Z.Z. contributed equally to this work. Y.Z. and N.P.P. conceived the idea. Y.Z. designed the experiments. Y.Z. conducted the synthesis of samples. Z.Z. conducted the solar-cells fabrication/testing. Y.Z. and Z.Z. performed the materials characterization (Optical, XRD, SEM, FTIR, PL, I-V scan, etc.) experiments. M.C. conducted AFM experiments. Y.Z. performed the TEM studies. All the authors contributed to the analysis of the data. Y.Z. and N.P.P. co-wrote the manuscript with comments and contributions from the other coauthors. The authors acknowledge the experimental assistance from W. Li, Dr. L. Zhang, and Dr. H. Khassaf. The authors also acknowledge Prof. Eiichi Nakamura for supporting Z.Z.'s contribution to this research. This research was supported by the National Science Foundation (OIA-1538893) and the Office for Naval Research (N00014-17-1-2232).

Conflict of Interest

The authors declare no conflict of interest.

Keywords

grain boundary, halide perovskites, solar cells, stability

Received: March 30, 2018

Revised: May 15, 2018

Published online:

- [1] J.-P. Correa-Baena, M. Saliba, T. Buonassisi, M. Grätzel, A. Abate, W. Tress, A. Hagfeldt, *Science* **2017**, *358*, 739.
- [2] a) M. Liu, M. B. Johnston, H. J. Snaith, *Nature* **2013**, *501*, 395; b) H.-S. Kim, C.-R. Lee, J.-H. Im, K.-B. Lee, T. Moehl, A. Marchioro, S.-J. Moon, R. Humphry-Baker, J.-H. Yum, J. E. Moser, *Sci. Rep.* **2012**, *2*, 591; c) A. Kojima, K. Teshima, Y. Shirai, T. Miyasaka, *J. Am. Chem. Soc.* **2009**, *131*, 6050.
- [3] Y. Zhou, O. S. Game, S. Pang, N. P. Padture, *J. Phys. Chem. Lett.* **2015**, *6*, 4827.
- [4] R. Prasanna, A. Gold-Parker, T. Leijtens, B. Conings, A. Babayigit, H. G. Boyen, M. F. Toney, M. D. McGehee, *J. Am. Chem. Soc.* **2017**, *139*, 11117.
- [5] W. Shockley, H. J. Queisser, *J. Appl. Phys.* **1961**, *32*, 510.
- [6] a) J.-W. Xiao, L. Liu, D. Zhang, N. De Marco, J.-W. Lee, O. Lin, Q. Chen, Y. Yang, *Adv. Energy Mater.* **2017**, *7*, 1700491; b) Y. Zhou, Z. Zhou, M. Chen, Y. Zong, J. Huang, S. Pang, N. P. Padture, *J. Mater. Chem. A* **2016**, *4*, 17623.
- [7] F. Hao, C. C. Stoumpos, R. P. Chang, M. G. Kanatzidis, *J. Am. Chem. Soc.* **2014**, *136*, 8094.
- [8] D. Zhao, Y. Yu, C. Wang, W. Liao, N. Shrestha, C. R. Grice, A. J. Cimaroli, L. Guan, R. J. Ellingson, K. Zhu, X. Zhao, R.-G. Xiong, Y. Yan, *Nat. Energy* **2017**, *2*, 17018.
- [9] W. Liao, D. Zhao, Y. Yu, N. Shrestha, K. Ghimire, C. R. Grice, C. Wang, Y. Xiao, A. J. Cimaroli, R. J. Cimaroli, R. J. Ellingson, N. J. Podraza, K. Zhu, R.-G. Xiong, Y. Yan, *J. Am. Chem. Soc.* **2016**, *138*, 12360.
- [10] X. Liu, Z. Yang, C.-C. Chueh, A. Rajagopal, S. T. Williams, Y. Sun, A. K. Y. Jen, *J. Mater. Chem. A* **2016**, *4*, 17939.
- [11] Z. Yang, A. Rajagopal, A. K. Y. Jen, *Adv. Mater.* **2017**, *29*, 1704418.
- [12] Z. Yang, A. Rajagopal, C. C. Chueh, S. B. Jo, B. Liu, T. Zhao, A. K. Y. Jen, *Adv. Mater.* **2016**, *28*, 8990.
- [13] J. Liu, G. Wang, Z. Song, X. He, K. Luo, Q. Ye, C. Liao, J. Mei, *J. Mater. Chem. A* **2017**, *5*, 9097.
- [14] Y. Zong, N. Wang, L. Zhang, M. G. Ju, X. C. Zeng, X. W. Sun, Y. Zhou, N. P. Padture, *Angew. Chem. Int. Ed.* **2017**, *56*, 12658.
- [15] D. P. McMeekin, G. Sadoughi, W. Rehman, G. E. Eperon, M. Saliba, M. T. Hörlantner, A. Haghighirad, N. Sakai, L. Korte, B. Rech, M. B. Johnston, L. M. Herz, H. J. Snaith, *Science* **2016**, *351*, 151.
- [16] I. Chung, J. H. Song, J. Im, J. Androulakis, C. D. Malliakas, H. Li, A. J. Freeman, J. T. Kenney, M. G. Kanatzidis, *J. Am. Chem. Soc.* **2012**, *134*, 8579.
- [17] N. Wang, Y. Zhou, M.-G. Ju, H. F. Garces, T. Ding, S. Pang, X. C. Zeng, N. P. Padture, X. W. Sun, *Adv. Energy Mater.* **2016**, *6*, 1601130.
- [18] Y. Zhou, M. Yang, W. Wu, A. L. Vasiliev, K. Zhu, N. P. Padture, *J. Mater. Chem. A* **2015**, *3*, 8178.
- [19] N. Ahn, D. Y. Son, I. H. Jang, S. M. Kang, M. Choi, N. G. Park, *J. Am. Chem. Soc.* **2015**, *137*, 8696.
- [20] a) A. G. Kontos, A. Kaltzoglou, E. Siranidi, D. Palles, G. K. Angeli, M. K. Arfanis, V. Psycharis, Y. S. Raptis, E. I. Kamitsos, P. N. Trikalitis, C. C. Stoumpos, M. G. Kanatzidis, P. Falaras, *Inorg. Chem.* **2017**, *56*, 84; b) M. H. Kumar, S. Dharani, W. L. Leong, P. P. Boix, R. R. Prabhakar, T. Baikie, C. Shi, H. Ding, R. Ramesh, M. Asta, M. Graetzel, S. G. Mhaisalkar, N. Mathews, *Adv. Mater.* **2014**, *26*, 7122.
- [21] C. Li, Y. Zhou, L. Wang, Y. Chang, Y. Zong, L. Etgar, G. Cui, N. P. Padture, S. Pang, *Angew. Chem. Int. Ed.* **2017**, *56*, 7674.
- [22] D. H. Kim, J. Park, Z. Li, M. Yang, J. S. Park, I. J. Park, J. Y. Kim, J. J. Berry, G. Rumbles, K. Zhu, *Adv. Mater.* **2017**, *29*, 1606831.
- [23] a) T. Liu, Y. Zhou, Z. Li, L. Zheng, M.-G. Ju, D. Luo, Y. Yang, M. Yang, D. H. Kim, W. Yang, N. P. Padture, M. C. Beard, X. C. Zeng, K. Zhu, Q. Gong, R. Zhu, *Adv. Energy Mater.* **2018**, <https://doi.org/10.1002/aenm.201800232>; b) Y. Zong, Y. Zhou, Y. Zhang, Z. Li, L. Zhang, M.-G. Ju, M. Chen, S. Pang, X. C. Zeng, N. P. Padture, *Chem.* **2018**, *4*, 1404.
- [24] a) F. Ji, S. Pang, L. Zhang, Y. Zong, G. Cui, N. P. Padture, Y. Zhou, *ACS Energy Lett.* **2017**, *2*, 2727; b) Y. Zhou, A. L. Vasiliev, W. Wu, M. Yang, S. Pang, K. Zhu, N. P. Padture, *J. Phys. Chem. Lett.* **2015**, *6*, 2292.
- [25] P. Xu, S. Chen, H.-J. Xiang, X.-G. Gong, S.-H. Wei, *Chem. Mater.* **2014**, *26*, 6068.
- [26] Z. Liu, J. Hu, H. Jiao, L. Li, G. Zheng, Y. Chen, Y. Huang, Q. Zhang, C. Shen, Q. Chen, H. Zhou, *Adv. Mater.* **2017**, *29*, 1606774.
- [27] a) M. Saliba, *Science* **2018**, *359*, 388; b) K. Domanski, E. A. Alharbi, A. Hagfeldt, M. Grätzel, W. Tress, *Nat. Energy* **2018**, *3*, 61.